batteries

MDPI

Article

When Electrolytes Are Semiconductors: A Feature, Not a Bug for Solid-State Batteries

Beatriz M. Gomes [1,2,3,†], Manuela C. Baptista [1,2,3,†] and M. Helena Braga [1,2,3,*]

[1] Faculty of Engineering, University of Porto, Rua Dr. Roberto Frias, 4200-465 Porto, Portugal; up201805007@up.pt (B.M.G.); up200501276@up.pt (M.C.B.)
[2] LAETA, Associated Laboratory of Energy, Transports and Aerospace, Rua Dr. Roberto Frias, 400, 4200-465 Porto, Portugal
[3] MatER, Materials for Energy Research Laboratory, University of Porto, Rua Dr. Roberto Frias, 4200-465 Porto, Portugal
* Correspondence: mbraga@fe.up.pt
† These authors contributed equally to this work.

Abstract

The development of stable and efficient solid electrolytes is essential for advancing solid-state battery technologies. In this study, we present a comparative study of three sulfide-based electrolytes, Li_6PS_5Cl (LPSCl), Li_6PS_5Br (LPSBr), and $Li_{10}GeP_2S_{12}$ (LGPS), combining Density Functional Theory (DFT) and hybrid (HSE06) simulations for electrochemical, charge carrier transport, and structural characterization. DFT and HSE06 simulations revealed semiconductor-like direct band gaps for LPSCl, with a 2.45 eV (DFT) −3.30 eV (HSE06) and 2.32 eV (DFT) −3.34 eV (HSE06) for LPSBr, and indirect band gap with 2.13 eV (DFT) −3.22 eV (HSE06) for LGPS, along with work functions of 3.40 eV for the argyrodites and 3.67 eV for LGPS. Scanning Kelvin Probe (SKP) analyses, performed at both micrometric and nanometric resolution, showed consistently negative surface potentials and interfacial polarons associated with electron tunneling through the surface of the electrolyte. Potentiostatic electrochemical impedance spectroscopy (PEIS) and cyclic voltammetry (CV) confirmed enhanced ionic conductivity with increasing temperature. While LPSCl and LGPS exhibited stable behavior at almost all temperatures, from −20 to 60 °C, LPSBr displayed noise-like activity at 0 °C with Au symmetric electrodes. This integrated experimental/theoretical approach highlights differences in electronic structure, interfacial charge distribution, and electrochemical stability, all showing affinity to react with lithium, providing key insights for the design and optimization of solid electrolytes for next-generation batteries.

Keywords: chemical potential; all-solid-state electrolytes; Sulfides; DFT simulations; semiconductors

Academic Editor: Yong-Joon Park

Received: 9 January 2026
Revised: 5 February 2026
Accepted: 7 February 2026
Published: 13 February 2026

1. Introduction

The urgent need for sustainability has placed renewable energy at the forefront, with batteries playing a critical role in achieving carbon neutrality and net-zero emissions [1]. All-solid-state batteries (ASSBs) offer transformative potential for electric vehicles (EVs), grid storage, and portable electronics by combining environmental and economic benefits [2]. By replacing the flammable liquid electrolytes, safety is improved, the environmental impact is reduced, and the demands for higher energy density and performance are met [3,4].

Solid-state electrolytes, a key component in ASSBs, are classified as inorganic solid electrolytes (ISEs) [5], polymer electrolytes (SPEs) [6], and solid composite electrolytes

(SCEs) [7]. ISEs, which include oxides (e.g., garnet [8] and LISICON [9]), sulfides (e.g., argyrodites [10] and thio-LISICON [11]), and halides (e.g., glassy electrolytes [12,13] and antiperovskite [14]), are distinguished by their high ionic conductivity, which is attributed to structural features such as defects in the crystal lattice, tunnels, and glass networks that enable efficient Li^+-ion transport, resulting in a cation transference number near one [7].

Sulfide-based solid-state electrolytes showcase exceptional Li^+-ion conductivity, often surpassing that of liquid electrolytes, but their commercialization faces significant challenges [15–17]. They include extreme moisture sensitivity leading to hydrolysis and toxic H_2S gas release, lithium polysulfide shuttling, mismatched interfaces, and chemical and electrochemical instabilities [2,4,18]. The natural abundance of sulfur, combined with its advantageous non-toxicity, enhances its suitability for industrial applications, offering significant economic potential [19].

In recent years, a growing number of scientific studies have focused on the development and characterization of the argyrodite-type solid electrolyte Li_6PS_5Cl (LPSCl). These investigations focus on the properties, such as ionic conductivity, structural stability, and electrochemical compatibility [20–30]. The highest reported ionic conductivity for LPSCl is 1.33 $mS{\cdot}cm^{-1}$ [31], while its electrochemical stability window reaches 7 V vs. Li/Li^+ [31] in a stainless-steel/LPSCl/Li cell, in which the 7 V likely includes the window of the solid electrolyte interphase SEI layer formed when the cell is charged 0.5 V above its open circuit voltage, therein referenced to 0 V. The activation energy values typical for this electrolyte are between 0.3 and 0.4 eV [31]. The Li_6PS_5Br (LPSBr) electrolyte has been the focus of studies for its high ionic conductivity, despite the toxic bromine [32–38] drawback. Thio-LISICON $Li_{10}GeP_2S_{12}$ (LGPS) has gained attention for its remarkable room-temperature ionic conductivity with a value of 12 $mS{\cdot}cm^{-1}$ [11], with an activation energy of approximately 0.22 eV [11,39,40]. Yet the high cost of the GeS_2 precursor presents a significant barrier to large-scale applications [20], making further research important to determine if its benefits outweigh the costs [41–46].

Computational methods, particularly based on Density Functional Theory (DFT) with hybrid functionals like HSE06, are essential tools in the literature for gaining fundamental atomic-scale insights that complement experimental characterization [47,48]. Ab initio methods enable the precise calculation of key electronic properties, including electronic band structure, density of states (DOS), and work functions, which are critical for understanding interfacial stability and charge transfer mechanisms in ASSBs. For sulfide-based electrolytes, DFT simulations have been widely employed to investigate ion transport [49,50], structural stability upon doping [49,50], and decomposition reactions at the interfaces [49,50]. Hybrid functionals like HSE06 are especially valuable as they correct the systematic band-gap underestimation inherent to standard DFT functionals, providing more accurate electronic descriptions essential for predicting band gaps, leading to a better description of the electrochemical windows [51].

This study focuses on three promising sulfide-based electrolytes—Li–argyrodites LPSCl and LPSBr, and LGPS—with the main goal of understanding the key factors behind their properties and determining the most adequate sulfide-based solid electrolyte for Li-based all-solid-state batteries. Ab initio simulations are used to study the chemical potential and band structure of these materials. Experimental methods, such as Scanning Kelvin Probe Microscopy (SKPM), electrochemical impedance spectroscopy (EIS), and cyclic voltammetry (CV) at different temperatures, are employed to confirm the simulation results and test the performance of these electrolytes in real applications (Figure 1). Throughout the manuscript, experimental results for the LPSCl, LPSBr, and LGPS electrolytes are represented using blue, pink, and green color palettes, respectively.

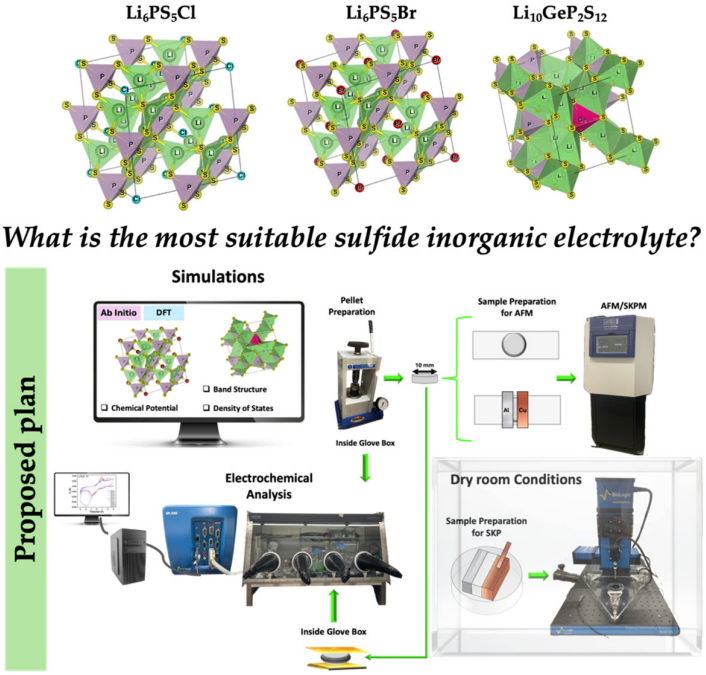

Figure 1. Top: crystal structures for the studied electrolytes—LPSCl [52], LPSBr [53] and LGPS [54]. Bottom: explanatory diagram of the simulations and experiments framework.

2. Results

2.1. Argyrodite—Li_6PS_5X, X = Cl, Br

The characterization of LPSCl and LPSBr was performed by analyzing their bulk electronic band structure, density of states (DOS), and electrical conductivity, and by calculating the work function of their simulated surfaces, Figure 2.

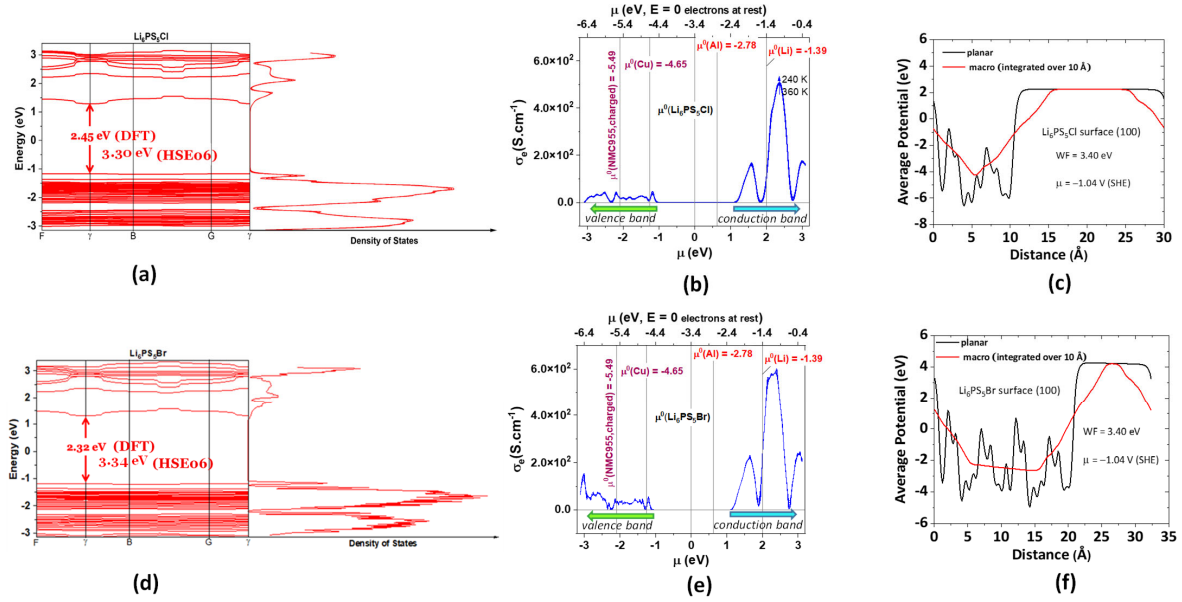

Figure 2. DFT simulations. Electronic band structures calculated along high-symmetry directions in the Brillouin zone, with highlighted band gaps, together with the corresponding density of states and simulated electrical conductivity during charge and discharge over a temperature range of 240–360 K (−33 to 87 °C): (**a**,**b**) LPSCl; (**c**) simulated chemical potential of LPSCl for the (100) surface; (**d**,**e**) LPSBr; and (**f**) simulated chemical potential of LPSBr for the (100) surface. Note: for the band gaps, the corrections were simulated with HSE06, showing 3.30 eV (LPSCl) and 3.34 eV (LPSBr).

The material exhibits a direct band structure, allowing electrons to transition between the valence and conduction bands through photon absorption without requiring a change in momentum.

Both LPSCl and LPSBr exhibit direct band gaps of 2.45 eV-DFT (3.30 eV-HSE06) and 2.32 eV-DFT (3.34 eV-HSE06), respectively, as shown in Figure 2a,d. These gaps' energy categorizes them as wide-band-gap semiconductors, with band gaps exceeding 2 eV. This property enables operation at higher voltages, frequencies, and temperatures, making them suitable candidates for advanced electronic and optoelectronic applications.

The density of states (DOS) profiles in Figure 2a,d show a clear correlation with the electrical conductivity data in Figure 2b,e, as expected. Electrical conductivity is strongly influenced by the availability of electronic states; regions with higher unoccupied DOS increase the probability of electron occupation and, thus, enhanced conductivity. In regions with low unoccupied DOS, conductivity decreases, further reinforcing the direct relationship between unoccupied DOS (Figure 2a,d) and electrical conductivity (Figure 2b,e). It is important to note that DOS reflects the availability, not the occupation, of electronic states. In Figure 2b,e, the chemical potentials (μ_0) of the LPSCl and LPSBr electrolytes are used as references, along with those of nickel manganese cobalt oxide $Ni_{0.90}Mn_{0.05}Co_{0.05}O_2$ (NMC955), copper (Cu) cathodes, and aluminum (Al) and lithium (Li) anodes.

The work functions of LPSCl and LPSBr do not differ and are equal to 3.40 eV, corresponding to a chemical potential of $\mu_0 = -3.40$ eV (considering the electrolytes are electrically insulated and do not show surface potential), as shown later in Figure 2c,f. The right-hand side of the gap in Figure 2b,e shows regions of higher electrical conductivity, therefore demonstrating that, provided the gap energy is available—for example, upon cell charging, leading to tunneling of electrons from the negative electrode to the electrolytes' surface—the electrolytes are reduced. Electrical conductivity is minimal in the fully occupied valence band and obviously zero within the band gap.

When a sufficiently high potential difference is applied ($\gtrsim$3.3 V) to the electrolytes, their conduction band begins to populate, allowing electrical conduction (Figure 2b,e). Lithium's chemical potential aligns with the electrolyte's conduction band; therefore, electron transfer becomes possible, facilitating electrolyte reduction. However, the density of states of LPSCl and LPSBr at or below the chemical potential of Li^0 is small, indicating that those states are easily filled, passivating the electrolytes. This transfer may occur via tunneling from the anode, not requiring an electric double layer, as the chemical potentials are equilibrated directly by charge transfer.

The work function of LPSBr for the (100) surface was determined to be 3.40 eV (Figure 2f). This value represents the minimum energy required to move an electron from the Fermi level to a point just outside the solid surface, where it comes to rest. The Fermi level in an insulator is forbidden. By definition, the probability of finding an electron at the Fermi level is ½, as the electrolyte is at lower temperatures as the valence band filled (probability 1), and the conduction band empty (probability 0). A similar work function of 3.40 eV has been reported for LPSCl on the same surface orientation (100) [55] (Figure 2c). When comparing LPSCl and LPSBr, it is important to consider their structural characteristics; both exhibit disordered structures, lacking long-range crystalline order, which allows for a range of atomic configurations. The substitution of Cl by Br results in a minor change in the ionic radius (approximately 6.5%), leading to minimal differences in electronic properties, such as the chemical potential and electrical conductivity.

Electrochemical characterization was performed using a Scanning Kelvin Probe (SKP) at both microscopic (Figures 3a–c and 4a–c) and nanoscopic scales (Figures 3d and 4d). At the microscopic level, SKP measurements of Cu/LPSCl/Al and Cu/LPSBr/Al cells revealed negative surface potentials for both electrolytes; −0.41 V for LPSCl (Figure 3a,c)

and −0.34 V and −0.57 V for LPSBr (Figure 4a,c) relative to the Standard Hydrogen Electrode (SHE) scale, and −4.10 and −3.87 eV in the absolute scale, which compare to −3.40 eV for the simulated value in (Figure 2c,f). The deviations are then −0.70, −0.47 V, where the experimental chemical potential has a higher "cathode character" than the simulated. This difference is much smaller when the circuit closes with a 1 kΩ resistor (LPSCl deviation: −0.19 V and LPSBr deviation: −0.22 V) and the electrons are allowed to be transported to/from the aluminum through the external circuit (Figures 3b and 4b). In the experiments without the external resistance (at open-circuit voltage, OCV), only the Cu is connected to the SKP. When the external resistor connects the circuit (Cu to Al), the Al electrode also becomes electrically connected to the SKP. As a result, both electrodes can shift toward their respective natural chemical potentials while the discharge is not predominant. The electrolyte, which previously had to compensate for the potential difference between the electrodes, relaxes toward its intrinsic potential, while the electrodes adjust to the electrolyte's chemical potential. Curiously, for the Cu/LPSCl/Al cell, the Al increases its chemical potential from −0.89 to −1.15 V vs. SHE (−3.55 to −3.29 eV) and the LPSCl from −0.41 to −0.85 V vs. SHE (−4.03 to −3.59 eV), which may indicate plasmonic transport through the surface of the LPSCl upon closing the circuit. We highlight that electrically insulated Al shows a chemical potential equal to −1.66 V vs. SHE. On the interface with Cu, the LPSCl raises its potential from −0.68 to −0.95 V vs. SHE (−3.76 to −3.49 eV) upon closing the circuit (Figure 3a,b); this latter value of the chemical potential of LPSCl only deviates −0.09 eV from the simulated value in Figure 2c, likely indicating that when the electrons are available, the chemical potentials evolve to assume their natural values. Curiously, the Cu—which receives electrons upon discharge through the external circuit, besides the exchange with the SKP—polarizes with a zone far from the interface at −1.07 V and a zone at the interface with LPSCl at −0.26 V vs. SHE, corresponding to a difference of ΔV = 0.81 V for Δx = 1430 μm; dV/dx = 566.4 μV.μm^{-1} (Figure 3b). Interestingly, the chemical potential of Cu at −1.07 V equalizes with the Al, separated by Δx = 9886 μm (Figure 3b). The chemical potential of the electrically insulated copper is ∼0.3 V vs. SHE, as shown in Figure 3a.

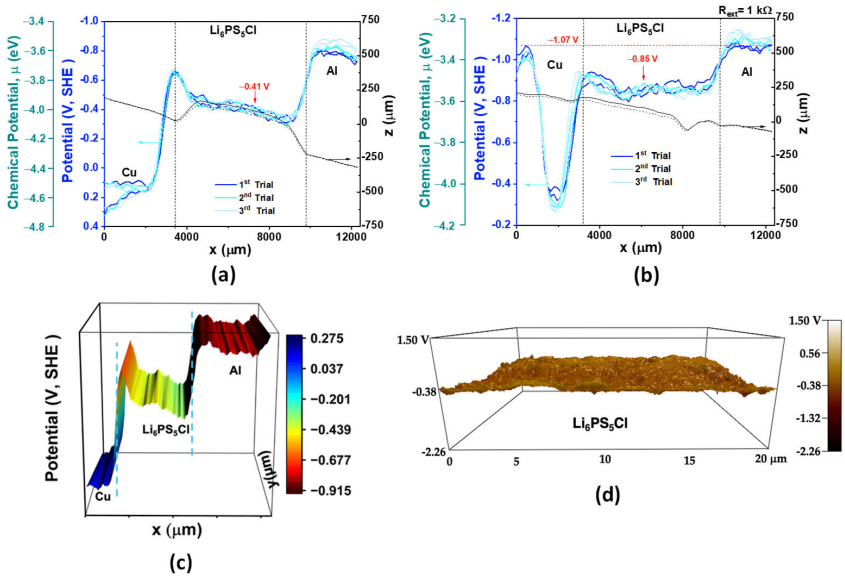

Figure 3. Electrochemical characterization. Scanning Kelvin Probe Microscopy (SKPM) with micrometric resolution for Cu/LPSCl/Al in (**a**,**b**), where (**a**) is without external resistor, (**b**) is with a 1 kΩ external resistor closing the circuit, and (**c**) is 3D. SKP with nanometric resolution on pellets of (**d**) LPSCl.

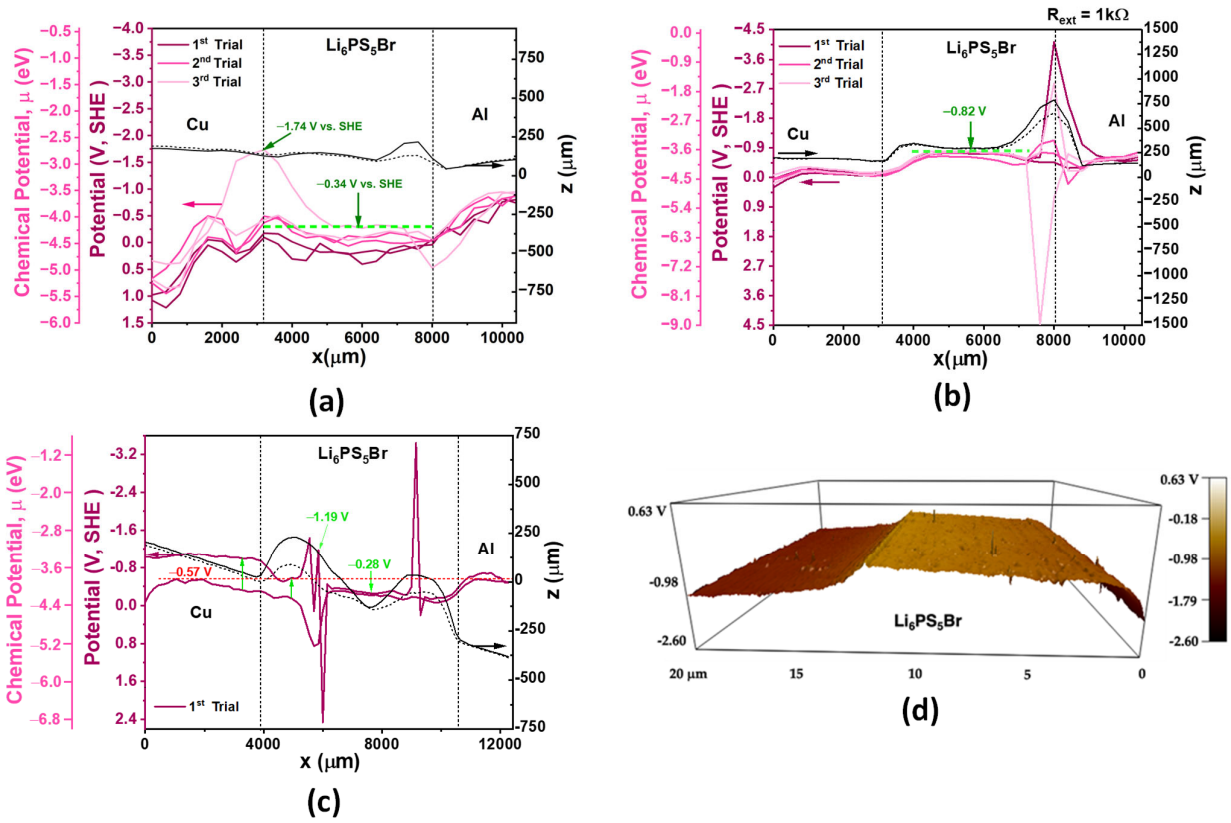

Figure 4. Electrochemical characterization. SKP analysis of the Cu/LPSBr/Al setup (**a**,**c**), where (**a**,**b**) are measured with a 400 μm/point resolution—(**a**) without external resistor, (**b**) with a 1 kΩ external resistor closing the circuit. (**c**) Scan at higher resolution, 150 μm/point, without external resistor. SKP with nanometric resolution on pellets of (**d**) LPSBr.

The LPSBr behaves as a semiconductor, exhibiting soliton-like features at the Cu–electrolyte interface (Figure 4a,c), which may correspond to negatively and positively charged species (electrons and holes or Li^+) [55]. These features could be associated with electron tunneling between electrode surfaces through the surface of the electrolyte, playing a critical role in enabling effective charge transfer in all-solid-state batteries. In a Cu/LPSBr/Al cell, Cu aligns directly with Al at −0.57 V, through a distance of Δx = 9231 μm (Figure 4c), very similar to the distance separating the equalized Cu and Al in the Cu/LPSCl/Al cell. When the Cu/LPSBr/Al cell is connected to a resistor of 1kΩ, the chemical potential of the electrolyte increases from −0.34 V vs. SHE to −0.82 V vs. SHE (−4.10 eV to −3.62 eV), Figure 4a,b, reducing the difference between the simulated chemical potential value (−3.40 eV) and the experimentally obtained values (Figures 2f and 4b). Additionally, like before with LPSCl, the Cu potential changed from −0.11 V vs. SHE to −0.22 V vs. SHE (−4.33 eV to −4.22 eV) and the Al from −0.55V to −0.85V vs. SHE (−3.89 eV to −3.59eV), indicating once again the occurrence of electron conduction through the surface of the electrolyte (Figure 4a,b).

From the nanometric SKP, pellets of LPSCl (Figure 3d) and LPSBr (Figure 4d) were analyzed. The potential response for insulated LPSCl obtained in Figure 3d was constant and approximately −0.38 V vs. SHE, consistent with that observed in Figure 3a away from the interfaces. For the LPSBr, the surface potential obtained by nanometric SKP was −0.98 V vs. SHE, similar to the simulation in Figure 2f.

To further evaluate the electrochemical performance of LPSCl and LPSBr, potentiostatic electrochemical impedance spectroscopy (PEIS) was performed on symmetrical Au/electrolyte/Au cells from 60 °C to −20 °C in 10 °C intervals (Figures 5a,d and 6a,d

and Table A1 in Appendix A). In this configuration, Au serves as a blocking electrode. For these cells, the high-frequency semicircle is attributed to the bulk ionic resistance of the electrolyte ($R_2 = R_{bulk}$), while the low-frequency response—irrelevant for diffusion at inert gold electrodes—was excluded from analysis. The data were modeled with an equivalent circuit of $R_1.(R_2//Q_2)$ (Table A1 in Appendix A). In this model, R_1 represents electrical and ionic resistance occurring independently at each interface, R_2 represents the bulk electrolyte resistance, and Q_2 is a pseudo-capacitance element representing the capacitance of the bulk capacitor with the same thickness as the electrolyte, where the interfacial phenomena do not contribute. The impedance of Q_2 is $Z_{Q_2} = \frac{1}{Q_2(j\omega)^n}$ where n is a phase exponent ($0 \leq n \leq 1$). Following this, cyclic voltammetry (CV) was performed on the same symmetrical Au/electrolyte/Au cells over the same temperature range of 60 °C to −20 °C in 10 °C intervals (Figures 5b,c and 6b,c and Table A1 in Appendix A). This setup allows evaluation of the solid electrolyte in a symmetric cell and enables assessment of its behavior against a dynamic cathode-like chemical potential material, such as gold. For both tests, electrolyte pellets were prepared by pressing 100 mg of each material under 1 ton for 1 min, after which they were placed between two gold electrodes for measurement inside an Ar-filled glovebox.

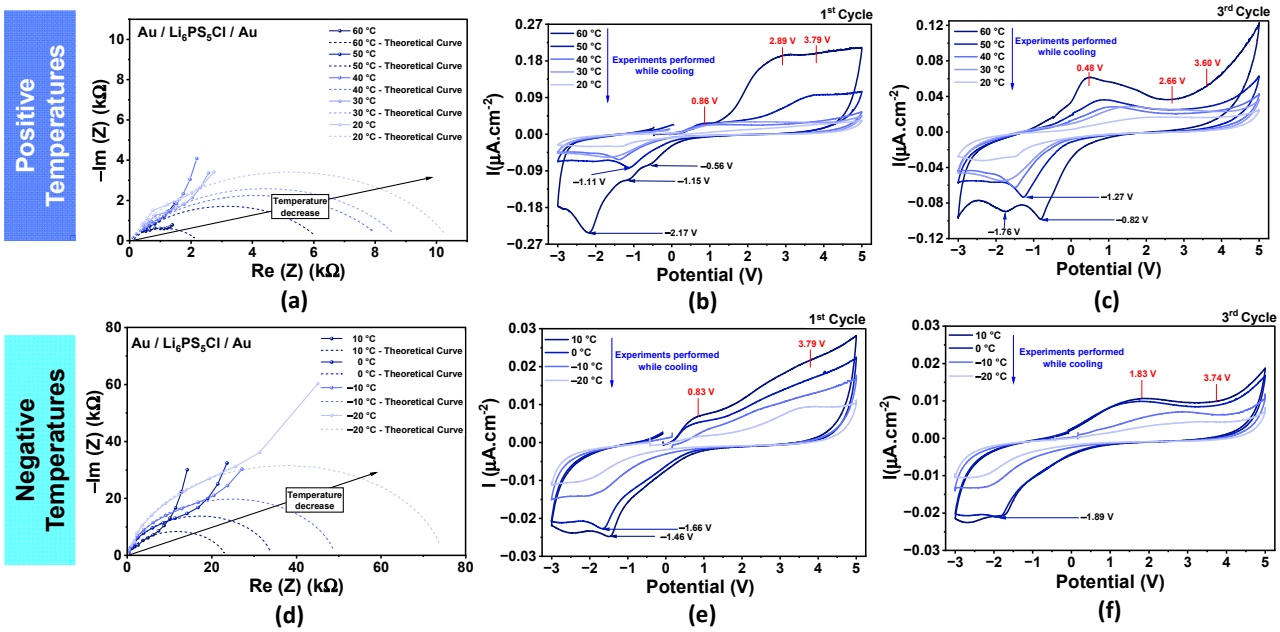

Figure 5. PEIS and CV analysis of LPSCl pellet with (Au) blocking electrodes, Au/LPSCl/Au. Top Part, positive temperatures, 60 °C, 50 °C, 40 °C, 30 °C, 20 °C: (**a**) comparative PEIS at different temperatures and comparative CV at different temperatures—(**b**) 1st cycle and (**c**) 3rd cycle. Bottom Part, below room temperature and negative temperatures, 10 °C, −0 °C, −10 °C, −20 °C: (**d**) comparative PEIS at different temperatures and comparative CV at different temperatures—(**e**) 1st cycle and (**f**) 3rd cycle.

As expected, increasing the temperature results in decreased impedance, consistent with enhanced ionic conductivity in an insulator (Figures 5a,d and 6a,d). For both electrolytes, when transitioning from 20 °C to 10 °C, a rise in the impedance is observed from $\sim 8 - 10$ kΩ to >20 kΩ, indicating that these electrolytes work better at temperatures above 20 °C, as expected (Table A1 in Appendix A). An interesting feature observed in the PEIS profiles was the presence of discontinuities across all temperatures, which may indicate the occurrence of different phenomena at distinct natural resonance frequencies (Figures 5a and 6a). To verify the reproducibility of this behavior, a second experimental setup was assembled, and the measurements were repeated at 25 °C and 40 °C under

identical conditions (Figure A1 and Table A2 in Appendix A). The discontinuities were consistently reproduced, supporting the existence of the so-called "forbidden pairs", as discussed later in the manuscript.

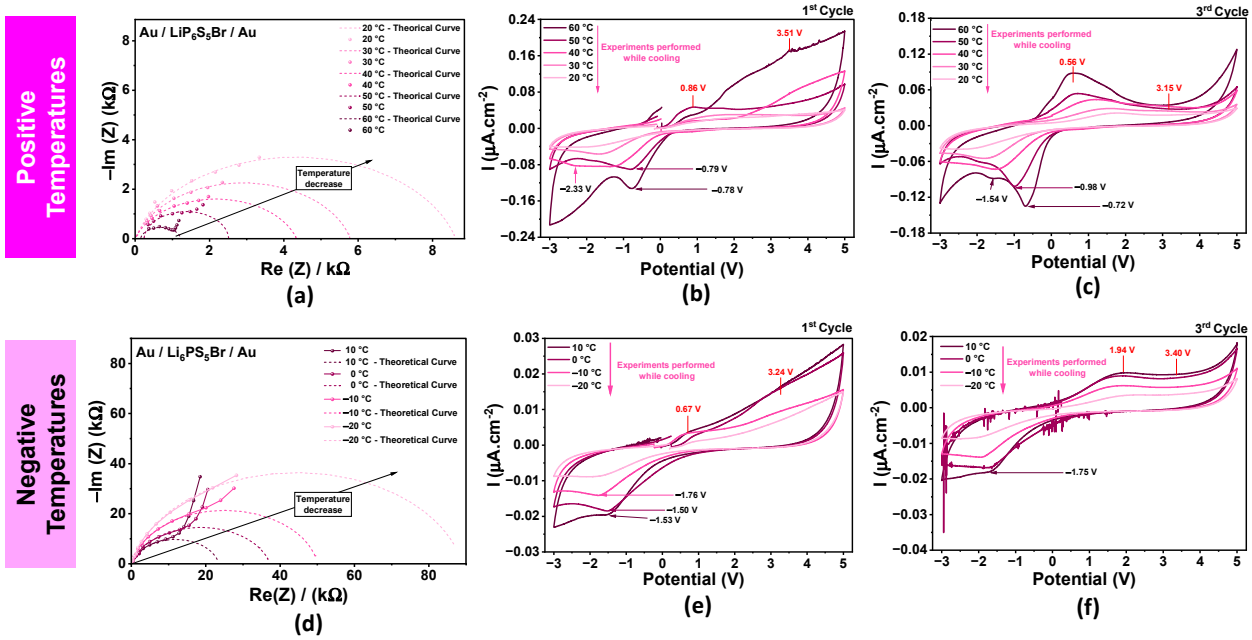

Figure 6. PEIS and CV analysis of LPSBr pellet with (Au) blocking electrodes, Au/LPSBr/Au. Top Part, positive temperatures, 60 °*C*, 50 °*C*, 40 °*C*, 30 °*C*, 20 °*C* : (**a**) comparative PEIS at different temperatures and comparative CV at different temperatures—(**b**) 1st cycle and (**c**) 3rd cycle. Bottom Part, below room temperature and negative temperatures, 10 °C, 0 °C, −10 °C, −20 °C: (**d**) comparative PEIS at different temperatures and comparative CV at different temperatures—(**e**) 1st cycle and (**f**) 3rd cycle.

Cyclic voltammetry (CV) shows that the current increases with temperature for both solid electrolytes, as shown in Figures 5b,c,e,f and 6b,c,e,f. Both electrolytes show a big difference in the CV curves between the first and third cycles at 60 °C, with a significant decrease in current from 0.21 to 0.12 μA.cm^{-2} for the LPSCl electrolyte and from 0.21 to 0.13 μA.cm^{-2} for the LPSBr, Figures 5b,c and 6b,c. These results indicate that some degradation may occur at this temperature after the first cycle, which could influence the current response in subsequent experiments since they were conducted while cooling. Across all tests, both electrolytes show an increase in current above 2.7–3.7 V, indicating a maximum operating voltage beyond which electrolyte degradation may occur, as seen in Figures 5b,c and 6b,c. This voltage will be shown hereafter to correspond to the minimum energy of conduction band, E_c of LPSCl and LPSBr. Regarding temperature effects, the CV profiles are similar for the following pairs: 50 °C and 40 °C; 30 °C and 20 °C; 10 °C and 0 °C; −10 °C and −20 °C. However, for the LPSBr, degradation is visible at 0 °C, as seen in Figure 6f. The noise observed in LPSBr, and not in LPSCl, could be related to structural transitions or heterogeneities in the Br^- crystalline sublattice due to a higher ionic radius. It is important to note that the peaks in Au//Au CV curves do not correspond to the typical oxidation and reduction peaks observed in conventional full/half cells with the structure cathode/electrolyte/anode. To better understand this behavior, test cells were assembled with the configuration NMC955/electrolyte /Li and subjected to CV analysis, with the results presented in Figure A2 (Appendix A). The electrochemical window employed in these tests is limited by the anode and cathode's position regarding the band gap of the electrolyte [17]. In the CV curves of these full cells, no distinct oxidation or

reduction peaks are observed, as the NMC955 cathode behaves as a solid-solution material, and there are minimal reactions between the electrolytes and NMC955, as will be discussed later. The inflection points in the discharge portion of the CV curves occur at 3.52 V for LPSCl (Figure A2, Appendix A). These points correspond to the characteristic "elbow" in the discharge profiles, consistent with previous observations [17].

The LPSCl electrolyte showed no detectable irreversible reactions across the investigated temperature range, indicating good thermal stability (Figures 5 and A1 in Appendix A). The LPSBr electrolyte exhibited a current peak at approximately 0.87 V at 25 °C (Figure A1 in Appendix A). At 40 °C, multiple peak currents were observed in Figure A1 in Appendix A, suggesting that the heating regime may be affecting the stability of the material more than cooling Figure 6b,c.

2.2. Thio-Lisicon—$Li_{10}GeP_2S_{12}$

The band gap analysis of LGPS demonstrates that the electrolyte has an indirect band gap of 2.13 eV-DFT (3.22 eV-HSE06), as shown in Figure 7a. This value, along with those of LPSCl and LPSBr, classifies these electrolytes as wide-band-gap semiconductors, with band gaps within the range $2 < E_g(eV) \leq 4.3$. Figure 7a shows a slightly smaller gap than LPSCl and LPSBr, see Figure 2a,d. In Figure 7b, the chemical potential (μ_0) of the LGPS electrolyte is used as a reference, along with those of NMC955, Cu, Al, and Li. In LGPS, the electrical conductivity of the electrons excited to the conduction band is approximately three times smaller than that of LPSCl, which does not really deviate considerably in its electrical properties when compared with the LPSCl and LPSBr, as the electrical conductivity of extremes such as Teflon (insulator) and graphene (conductor) differ by 25–30 orders of magnitude [56].

The work function of LGPS for the (001) surface was determined to be 3.67 eV (Figure 7c), slightly higher than the value obtained for LPSCl and LPSBr (Figure 2c,f). The SKP measurements performed on the Cu/LGPS/Al cell are shown in Figure 7d–f. Figure 7d,e were acquired with a spatial resolution of 400 µm/point; Figure 7d corresponds to the Cu/LGPS/Al configuration, while Figure 7e shows the same cell connected to an external 1 kΩ resistor. The chemical potentials of Cu and Al were measured as +0.21 V vs. SHE (−4.23 eV) and −0.72 V vs. SHE (−3.72 eV), respectively (Figure 7d). The LGPS electrolyte exhibited a chemical potential of −0.44 V vs. SHE (−4.00 eV) under open-circuit conditions (Figure 7d). When the cell was connected to the external resistor (Figure 7e), shifts in the chemical potentials of all components were observed: Cu shifted to +0.55 V vs. SHE (−4.99 eV), Al to −0.84 V vs. SHE (−3.60 eV), and LGPS to −0.21 V vs. SHE (−4.23 eV). A systematic evolution of the chemical potential is observed for all materials in the cell from the first to the third trial, characterized by a uniform decrease of approximately 0.2 V vs. SHE (Figure 7e). Despite this global shift in absolute potential for Cu, the electrolyte, and Al, the relative potential differences between the materials remain unchanged. The chemical potential of Al shows the same tendency as what was observed in the cells with LPSCl and LPSBr. However, Cu and LGPS exhibit the opposite trend, although as the copper is connected to the SKP, the analysis is not correct, and therefore we cannot make a direct comparison to the cell properties; the chemical potential of Cu becomes more positive (from 0.21 to 0.55 V vs. SHE), and that of LGPS shifts from −0.44 to −0.21 V vs. SHE, indicating once again that electrons are transported along the surface from Al toward Cu through the LGPS. In contrast, in the LPSCl and LPSBr cells, electron conduction appears to proceed from Cu through the electrolyte surface toward Al, as mentioned before.

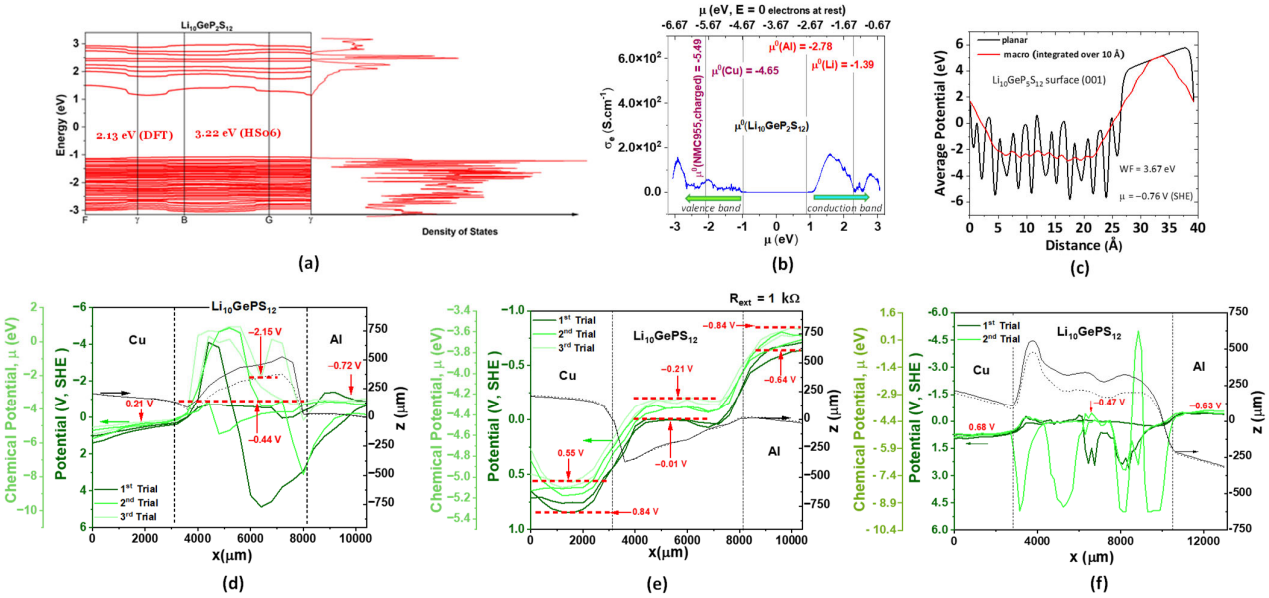

Figure 7. DFT simulations and electrochemical characterization: (**a**) Electronic band structure along high-symmetry directions in the Brillouin zone with highlighted band gap 2.13 eV - DFT (3.22 eV - HSE06) and density of states for $Li_{10}GeP_2S_{12}$. (**b**) Simulated electrical conductivity while cycling (charge and discharge) from 240 to 360 K (−33 to 87 °C). (**c**) Work function and chemical potential of LGPS. Electrochemical characterization using Scanning Kelvin Probe Microscopy (SKPM) with micrometric resolution 2D SKP surface potential map of a Cu/LGPS/Al configuration (**d**) without external resistor and (**e**) with a 1 kΩ external resistor closing the circuit, both measured at a resolution of 400 μm/point. (**f**) Scan at higher resolution, 150 μm/point, without external resistor.

To obtain higher-resolution data, the Cu/LGPS/Al cell was remeasured under open-circuit conditions (without the external resistor) at 150 μm/point (Figure 7f). The Cu surface potential increased to +0.68 V vs. SHE (−5.12 eV) (Figure 7f) from its standard value of +0.30 V vs. SHE (−4.74 eV) measured in the Cu/LPSCl/Al cell (Figure 3a), while the Al surface potential shifted from −0.87 V vs. SHE (−3.57 eV) in Cu/LPSCl/Al (Figure 3a) to −0.63 V vs. SHE (−3.81 eV) in the Cu/LGPS/Al system (Figure 7f).

This indicates that Cu acted as an electron donor, whereas Al not only did not receive these electrons, but may even have released electrons to the surface of the electrolyte LGPS. The average LGPS surface potential is −0.44 V vs. SHE (−4.00 eV) (Figure 7d); however, several potential peaks that are especially negative, but also positive, are observed, indicating that the electrolyte surface functions as a transport medium, enabling polarons–electrons and holes or Li^+- exchanges between the electrodes (Figure 7f), which results in a reduction in the potential bias between the electrodes. This behavior, demonstrated in Figure 7d,f, was previously observed for LPSCl [55] and LPSBr electrolytes in (Figure 4b,c). The experimental chemical potential deviated from the simulated value by 0.32 eV, where the simulated value is placed more to the "anode side" of the absolute scale.

To further evaluate the electrochemical performance of LGPS, PEIS and CV were conducted over a temperature range from 60 °C to −20 °C in 10 °C intervals (Figure 8 and Table A1 in Appendix A). As observed previously for the LPSCl and LPSBr, increasing the temperature leads to a reduction in impedance, consistent with enhanced ionic conductivity expected from higher temperatures (Table A1 in Appendix A). At 60 °C, the CV results show a decrease in current from the first to the third cycle, similar to what was observed for LPSCl and LPSBr (LGPS: Figure 8b,c; LPSCl: Figure 5b,c; LPSBr: Figure 6b,c). This suggests that irreversible reactions, likely associated with electrolyte degradation, occur during the initial cycle at elevated temperatures. At 50 °C, 40 °C, 30 °C, and 20 °C, degradation signatures appear at negative voltages, indicating that the electrolyte does not

remain electrochemically stable in this temperature range (Figure 8b,c). However, at negative temperatures, LGPS displays improved stability compared with the argyrodite electrolytes exhibiting higher current responses (LGPS: Figure 8e,f; LPSCl: Figure 5e,f; LPSBr: Figure 6e,f). Complementary experiments on additional Au/LGPS/Au cells confirmed the same overall trends (Figure A1 and Table A2 in Appendix A). These results also suggest that LPSCl and LPSBr exhibit the highest conductivity when the electrons are excited to the conduction band, as shown in Figure A2 in Appendix A.

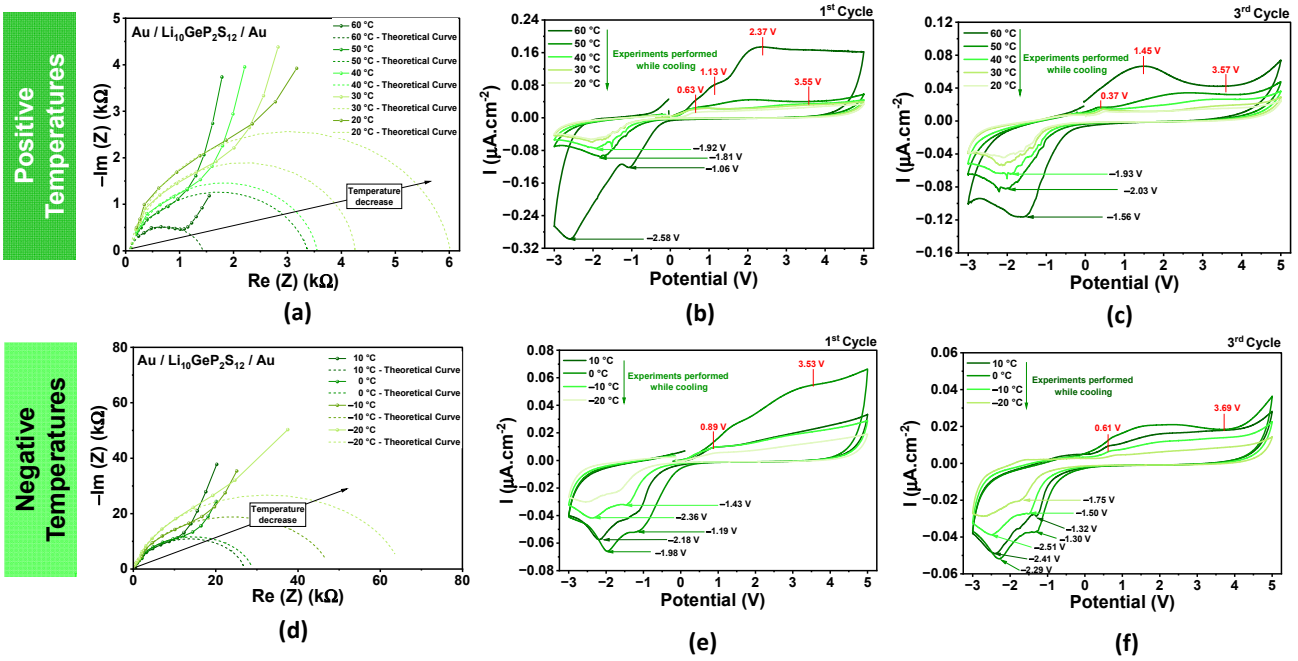

Figure 8. PEIS and CV analysis of LGPS pellet with (Au) blocking electrodes, Au/ LGPS/Au. Top Part, positive temperatures, 60 °C, 50 °C, 40 °C, 30 °C, 20 °C: (**a**) comparative PEIS at different temperatures and comparative CV at different temperatures—(**b**) 1st cycle and (**c**) 3rd cycle. Bottom Part, below room temperature and negative temperatures: (**d**) comparative PEIS at different temperatures and comparative CV at different temperatures—(**e**) 1st cycle and (**f**) 3rd cycle.

For all the electrolytes tested in this study, the PEIS exhibit discontinuities that correspond to different phenomena occurring at distinct resonance frequencies (Figure 9). There is a clear tendency for presenting two discontinuities observed on all the electrolytes at different temperatures, with the exception of LGPS, which at 60 °C does not show any discontinuities. These breaks may be due to a change in resonance frequencies attributed to different species inside the electrolyte (Figure 9). These apparent "jumps" arise from a combination of non-linear interfacial effects (such as space-charge or ionic accumulation at blocking electrodes) and microstructural heterogeneities (including grain boundaries and imperfect contact), rather than from a purely linear bulk dielectric response. This phenomenon is apparently similar to that reported for the ferroelectric electrolytes $A_{2.99}Ba_{0.005}OCl$ [57], where (A = Li, Na, and K).

The corresponding resonant and forbidden frequencies are very similar for all the studied electrolytes (Figure 9). To higher frequencies, at the same temperature, correspond lower impedances; there is a forbidden zone of pairs (frequency and impedance) demonstrated in Figure 9, similar to the one shown in [57], highlighting the occurrence of non-linear damped and forced oscillators. The LPSCl and LPSBr electrolytes exhibit similar trends regarding their forbidden frequencies (Figure 9a,c). There is no distinct correlation between the relaxation of these forbidden zones and temperature; this observation aligns with the CV data (Figures 5 and 6), where the electrochemical behavior remains nearly identical

across the positive temperature range. In contrast, LGPS displays a significantly linear profile in its forbidden frequencies (Figure 9b,d). These forbidden zones remain stable and similar across all temperatures except 60 °C, like that observed for the CV (Figure 8).

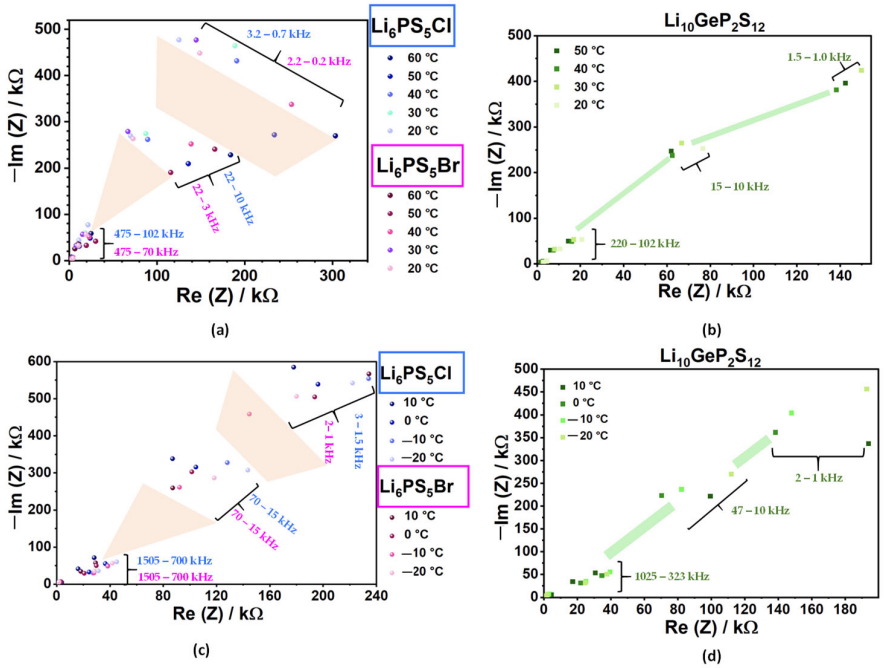

Figure 9. Comparison between the impedance discontinuities as a function of frequency. −Im (Z) vs. Re (Z). Top Part, positive temperatures, 60 °C, 50 °C, 40 °C, 30 °C, 20 °C: (**a**) argyrodite electrolytes, (**b**) *Thio-Lisicon*. Bottom Part, below room temperature and negative temperatures, 10 °C, −0 °C, −10 °C, −20 °C: (**c**) argyrodite electrolytes, (**d**) Thio-Lisicon.

The concluding schematics in Figure 10a show that, even if the electrolytes are semiconductors, it may not bring an impediment to being used in all-solid-state cells. With reference to the charged NMC_{955} cathode, the LGPS will be the electrolyte less prone to form a solid interphase by electron tunneling from the valence band of the LGPS to the accepting bands of the NMC conductor, while the electrolyte is charged. However, none of the electrolytes will show extended reactions with the NMC as the maximum energy of the valence band of the electrolytes is very similar to the chemical potential of the NMC, $E_V(\text{electrolytes}) \approx \mu_{NMC955} = -5.49$ eV (charged). When the NMC_{955} cathode discharges, the chemical potential raises to −3.99 eV (2.6 V vs. SHE) for $LiNi_{0.90}Mn_{0.05}Co_{0.05}O_2$ and no tunneling of electrons from the electrolytes to the NMC_{955} occurs.

The LFP will not show spurious reactions at the cathode side of the interface with any of the electrolytes, as the plateau chemical potential of the reaction between $LiFePO_4$ and $FePO_4$ with $\mu_{LiFePO4} = \mu_{FePO4} = -4.84$ eV is higher than the valence band of all the electrolytes, which are full and, therefore, will not receive electrons from the LFP.

In a Li-anode battery cell, electrons are prone to tunnel from the Li at −1.39 eV to the conduction band of LPSCl ($E_c \geq -1.75$ eV), LPSBr ($E_c \geq -1.73$ eV), and LGPS ($E_c \geq -2.06$ eV), although the reaction should not be too relevant for LPSCl and LPSBr, as the difference between the chemical potential of the Li and the minimum energy of the conduction band is 0.36 eV (LPSCl) and 0.34 eV (LPSBr), rapidly compensated by a small leakage current, eventually forming an SEI layer. The $\mu(\text{Li}) - E_{c,\text{minimum}}(\text{LGPS}) = 0.67$ eV requires a higher leakage current to compensate for the difference between chemical potentials of the $\mu(\text{Li}) = -1.39$ eV and $\mu(\text{LGPS}) = -3.67$ eV, likely forming an SEI. The SEI passivates the anode, and its thickness is regulated by the previously described process that drives it. As soon as an insulator interphase with higher E_c than $\mu(\text{Li})$ forms at the interface

Li//electrolyte, the electron tunneling to the E_c of the electrolyte drastically reduces its probability.

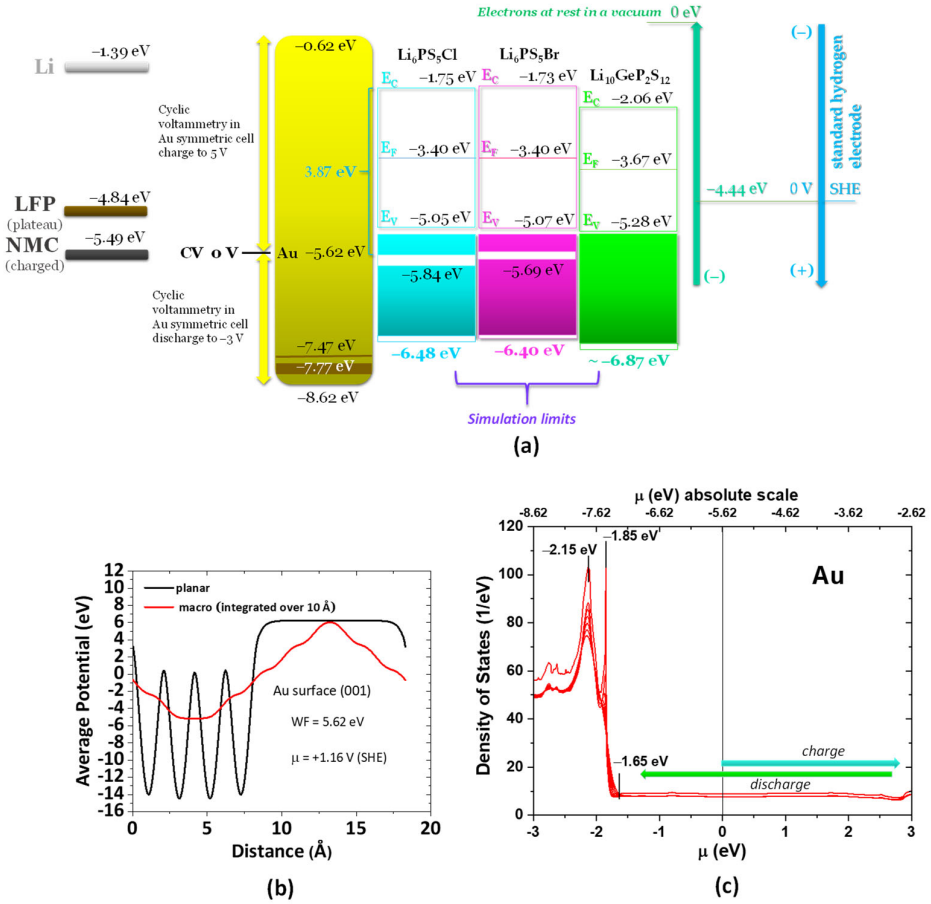

Figure 10. Relative positions of the chemical potentials, valence bands, conduction bands and energy gaps of the LPSCl, LPSBr, and LGPS electrolytes versus Li–metal anode, $LiFePO_4$ (LFP), and $Li_{0.27}Ni_{0.90}Mn_{0.05}Co_{0.05}$ (NMC) cathodes and gold (Au). E_C = minimum energy of the conduction band; E_F = Fermi level corresponding to the electrochemical potential that corresponds to the chemical potential of the insulated materials that do not show surface potentials; E_V = maximum energy of the valence band. (**a**) Comparative schematics. (**b**) Work function obtained after simulating average potential of Au in a (001) surface. (**c**) Density of states (DOS) vs. the chemical potential of Au while cycling.

In cyclic voltammetry with a gold symmetric cell, Au/electrolyte/Au, one gold plate is being charged and the opposite discharged; however, as the reference is connected to the working electrode, the voltage corresponds to the potential of the working electrode.

The electrochemical potential or chemical potential of the electrically insulated gold (Au) is calculated in Figure 10b after simulation of the (001) surface. The corresponding density of states DOS was also simulated and shown in Figure 10c.

A peak is expected at −0.57/0.57 V, corresponding to the difference between the chemical potential the μ(Au) and the E_V of LPSCl, −5.62 eV (Au) + 5.05 eV (LPSCl); because the chemical potential of the Au is smaller than the maximum energy of the valence band of the LPSCl in the absolute scale, the LPSCl gives away electrons to Au at OCV until the gold is charged to 5.05 eV or discharged from 5.05 eV to its natural chemical potential, μ(Au) = −5.62 eV (Figure 10a,b). The cell in Figure 5b,c is reasonably symmetric, and the values of the just-discussed peaks are obtained via CV at −0.56/+0.86 V (first cycle) and −0.82/+0.48 V (third cycle) at 60 °C. Below room temperature, the peak is only observed at

+0.83 V at 10 °C, Figure 5e. However, the CV is far from equilibrium at 50 $mV.s^{-1}$, especially at low temperatures, where the ionic transport takes more time.

For LPSBr, the expected peaks are −0.55/0.55 V with no correction for the OCV ∼ 0 V. The CV of Au/LPSBr/Au shows −0.78/0.86 V (first cycle, Figure 6b) and −0.56/0.72 V (third cycle, Figure 6c) at 60 °C, which is in good agreement with the simulated values. At negative temperatures, the peak observed is +0.67 V from 10 to −10 °C, as seen in Figure 6e.

For LGPS, the expected peaks are −0.34/0.34 V with no correction for the OCV ∼ 0 V. The CV of Au/LGPS/Au shows +0.63 V (first cycle, Figure 8b) and +0.37 V (third cycle, Figure 6c) for T ≤ 60 °C, which is in good agreement with the simulated values. No corresponding negative peaks are found, maybe due to the dynamics of the CV analyses and some possible hysteresis. Below room temperature and at negative temperatures, the peaks observed are +0.89 V (first cycle, Figure 8e) and +0.61 V (third cycle, Figure 8f).

When the chemical potential of gold rises above the E_c of the electrolytes, the gold may start reducing the electrolyte by direct electron tunneling to the E_c that is expected when the working electrode at Au/LPSCl/Au is charged to 3.87 V; Au/LPSBr/Au to 3.89 V; and Au/LGPS/Au to 3.56 V. Above these voltages, while charging the working electrode, the current should increase and instabilities may be observed due to the reduction in the electrolyte. In fact, the corresponding voltages for Au/LPSCl/Au are observed at approximately 2.89–3.79 V (Figure 5b), 2.66–3.60 V (Figure 5c), 3.79 V (Figure 5e), and 3.74 V (Figure 5f). For the Au/LPSBr/Au cell, the characteristic voltages are observed at approximately 3.51 V (Figure 6b), 3.15 V (Figure 6c), 3.24 V (Figure 6e), and 3.40 V (Figure 6f). For the Au/LGPS/Au cell, the characteristic voltages are observed at approximately 3.55 V (Figure 8b), 3.57 V (Figure 8c), 3.53 V (Figure 8e), and 3.69 V (Figure 8f).

The latter voltages indicate that the simulations and calculations of the chemical potentials and band structures are accurate. Our results confirm that LPSCl, LPSBr, and LGPS have a semiconducting nature, which we identify as a favorable characteristic for solid electrolyte performance as they favor the formation of an SEI layer necessary for efficient anode passivation. Notably, this behavior is not unique to these materials [4]. Recent studies have reported similar semiconducting and wide-band-gap semiconducting behavior across a broader class of lithium- and sodium-based solid electrolytes. Examples include LAGP, NASICON, LLZO, LLTO, Li_3OCl, Na_3OCl, K_3OCl, Li_3InCl_6 and Li_3ZrCl_6 [4]. Many of these electrolytes represent state-of-the-art materials and have demonstrated strong performance in practical, real-world applications [4].

When the Au working electrode discharges below the valence band E_v of the electrolyte, electrons may tunnel from the electrolyte to the electrode. Where Au shows a higher DOS (Figure 10c), the current in the CV should show a peak. In this case, at least two peaks should be similar for all the electrolytes as they depend on the Au, at −1.65 V, and especially at −1.85 and −2.15 V. The experimental data from the CVs are now generally as or more accurate at lower temperatures, as the Au electrode will conduct better at lower temperatures and will not react irreversibly. In particular, the peaks mentioned are −1.11 to −1.15 V and −2.17 V in Figure 5b, −1.27 and −1.76 V in Figure 5c, −1.46 to −1.66 V in Figure 5e, and −1.89 V in Figure 5f for the Au/LPSCl/Au cell; −2.33 V in Figure 6b, −1.54 V in Figure 6c, −1.50 to −1.76 V in Figure 6e, and −1.75 V in Figure 6f for the Au/LPSBr/Au cell; and −1.81 to −1.92 V and −2.58 V in Figure 8b, −1.56 to −2.03 V in Figure 8c, −1.19 to −1.43 V and −1.98 to −2.36 V in Figure 8e, and −1.30 to −1.75 and −2.29 to −2.51 V in Figure 8f for the Au/LGPS/Au cell. Herein, again, all the simulations are identically coherent with the experimental data. We highlight that the internal resistances in the CV cycles were not accounted for; therefore, the data verify the predicted results with close agreement.

3. Materials and Methods

Three different electrolyte materials were studied: Li_6PS_5Cl (MSE Supplies®, Tucson, AZ, USA) with a particle size pass 150 mesh $\leq$ 100 µm, Li_6PS_5Br (MSE Supplies®, Tucson, AZ, USA) with a particle size (D_{50}) of approximately 10 µm (sieved through a 325 mesh), and $Li_{10}GeP_2S_{12}$ (MSE Supplies® , Tucson, AZ, USA) with a particle size (D_{50}) of 10 µm (also sieved through a 325 mesh) and a purity exceeding 99.9%.

Pellets 10 mm in diameter and with ~1 mm thickness (~100 mg) were fabricated by compressing the material at 1 ton of pressure for 1 min using a SPECAC press. These pellets were subsequently analyzed using potentiostatic electrochemical impedance spectroscopy (PEIS), cyclic voltammetry (CV), and Atomic Force Microscopy (AFM). PEIS and CV analyses were performed using a Biologic SP-240 (BioLogic Corporation, Seyssinet-Pariset, France). potentiostat inside a GS Glove Box (O_2 < 0.1 ppm, H_2O < 0.1 ppm). The electrolyte pellets were placed between two gold plates (Thermo scientific, gold foil, 0.5 mm thick, 99.95% metal basis, 25 × 25 mm). Measurements were conducted in the sequence PEIS–CV at different temperatures: 60 °C, 50 °C, 40 °C, 30 °C, 20 °C, 10 °C, 0 °C, −10 °C, −20 °C. PEIS measurements were initiated at a frequency of 7 MHz and recorded for decreasing frequencies to 100 mHz. CVs were conducted at a scan rate of 50 $mV.s^{-1}$, from −3V to 5V. AFM analysis was performed in an Oxford Instruments Atomic Force Microscope MFP-3D Origin+ AFM (Asylum Research, Oxford Instruments, Santa Barbara, CA, USA), with the capability of performing Scanning Kelvin Probe Microscopy (SKPM). The tests were carried out using a laser-driven tip ASYELEC-01-R2 with resonant frequency of approximately 75 kHz. The tip material comprised silicon with a reflective coating of Ti/Ir and a spring constant (k) of 2.8 $N.m^{-1}$. The electrolyte pellets were fixed to a glass slide using insulating tape and then were tested.

Another approach involved using the electrolyte powders to assemble prototype cells with configuration Cu/electrolyte powder/Al for Scanning Kelvin Probe (SKP) measurements in a Biologic SKP-M470 (BioLogic Corporation, Seyssinet-Pariset, France) using a SKP probe U-SKP-370/1 made of tungsten wire with 500 µm diameter. The distance between the probe tip and the sample was ~200 µm, with the analysis monitored via a camera. All SKP experiments were conducted in a dry box continuously purged with argon and connected to a vacuum pump during all measurements. This study uses the methods described in [55,58].

Simulations were conducted to support experimental calculations. Density Functional Theory (DFT) and hybrid functional (HSE06), as implemented in VASP (version 6.3.2; VASP Software GmbH, Vienna, Austria) [59] and MedeA (version 3.7.0; Materials Design, Inc., San Diego, CA, USA) [60], were used to optimize the crystal structures of LPSBr and LGPS, following the approach reported by the authors [55] for LPSCl. The employment of hybrid functional, HSE06, was to obtain accurate values of band gap, which are known to be underestimated by DFT in semiconductors.

The simulations were first performed using DFT with the GGA-PBE exchange–correlation functional. We highlight that semi-local DFT (LDA/GGA) systematically underestimates semiconductor band gaps because of self-interaction errors and the missing derivative discontinuity in the exchange–correlation functional, typically by ~30–70% (~0.5–2 eV). Herein, the deviations to the values obtained by HSE06 were 74% (LPSCl), 69% (LPSBr), and 66% (LGPS).

The simulations used plane-wave cutoffs of ~500 eV (499.034 eV), reciprocal-space projections where applicable, and k-point spacing of 0.2–0.3 Å (0.208 × 0.213 × 0.207 $Å^{-1}$ for LPSCl, 0.124 × 0.126 × 0.124 $Å^{-1}$ for LPSBr, 0.176 × 0.186 × 0.160 $Å^{-1}$ for LGPS). Energies of formation, internal pressures, and atomic trajectories were monitored to ensure structural stability. Following the optimization of atomic positions, volume, and shape,

Boltzmann transport properties [61]—such as electronic band structure, density of states, and electrical conductivity—were simulated as a function of the chemical potentials and temperature. To calculate the work functions and compare electrolytes, we have also simulated (100) surfaces for the disordered structures after substitutions in the periodic ordered structures of LPSCl (cubic argyrodite, space group F-43m), LPSBr (cubic argyrodite, space group F-43m), and LGPS (tetragonal, space group $P4_2/nmc$). The Au (cubic space group F-43m) structure was also optimized, and, subsequently, the (001) surface work function, which allowed us to calculate the chemical potential and DOS (Figure 10).

4. Conclusions

In this study, we performed a comparative analysis of three solid electrolytes, LPSCl, LPSBr, and LGPS, combining ab initio simulations with advanced electrochemical characterization techniques to evaluate electronic, potential, and interfacial properties.

In the literature, electrolytes are generally expected to behave as insulators; however, these three highly promising solid electrolytes are all wide-band-gap semiconductors like other real-world performing electrolytes. The semiconductor character of the electrolytes benefits the formation of an efficient SEI layer at the anode interface that favors the performance of the batteries.

SKP measurements provided detailed insights into surface potentials and interfacial charge distributions. Pronounced potential (V) oscillations near the metal/electrolyte interfaces suggested electron tunnelling and soliton-like features in LPSCl and LPSBr, indicative of surface conduction through the electrolyte. LGPS also displayed negative average potential and more pronounced positively and negatively charged surface regions, consistent with its more pronounced semiconducting character.

All PEIS spectra for the different solid-state electrolytes showed distinct discontinuities associated with different resonances and forbidden processes. CV measurements demonstrated the electrochemical stability of all electrolytes at all temperatures, with no significant reaction peaks observed.

Overall, the integration of ab initio simulations with experimental measurements provides a comprehensive understanding of the fundamental properties of these solid electrolytes and their relative properties compared to cathode-like NMC955, Cu, and Au, and anode-like Al and Li. The combined results disclose the superior thermal and electrochemical stability of LPSCl, the interfacial complexity of LPSBr, and the distinct electronic features of LGPS.

Understanding the cyclic voltammetry of symmetric Au/all-solid-state electrolytes/Au is achieved herein for the first time by referring to chemical potential simulations, DOS, and transport properties for all materials involved.

As a conclusion, the parameters that count as an advantage besides cost, sustainability, and reactivity in ambient conditions, are: (1) electrical conductivity in the conduction band (when charged); (2) relative position of the lower energy of the conduction band regarding the anode (e.g., Li^0), as this influences the formation of the SEI and redox currents. Taking these factors into consideration, the electrolyte that is likely the best choice for being used in Li-metal batteries is LPSCl.

The present multimodal characterization approach offers critical insights for guiding the optimization of solid-state electrolytes—for example, by mixing with other electrolytes or other insulator materials—and supports the development of more efficient and stable materials for solid-state battery applications.

Author Contributions: Data curation, formal analysis, and software, B.M.G., M.C.B., and M.H.B.; writing—original draft preparation, B.M.G. and M.C.B.; investigation and methodology, B.M.G., M.C.B., and M.H.B.; conceptualization, funding acquisition, project administration, simulations, supervision, validation, visualization, and writing—review and editing, M.H.B. All authors have read and agreed to the published version of the manuscript.

Funding: This project received funding from the European Union's Horizon Europe research and innovation program, grant agreement No. 101069686 (PULSELiON); and the Portuguese Foundation for Science and Technology, FCT UID/50022/2025—LAETA (LT06).

Data Availability Statement: Data are available upon reasonable request.

Conflicts of Interest: The authors declare no conflicts of interest. The funders had no role in the design of the study; in the collection, analyses, or interpretation of data; in the writing of the manuscript; or in the decision to publish the results.

Appendix A

Table A1. Theoretical parameters obtained by fitting experimental data associated with LPSCl (Figure 5a,d), LPSBr (Figure 6a,d), and LGPS (Figure 8a,d).The equivalent circuit was discussed in the main manuscript.

Electrolytes	Temperature (°C)	R_1 (Ω)	C_2 (pF)	R_2 (kΩ)
Li_6PS_5Cl	60	0	42	2.2
	50	102	136	6.1
	40	0	118	6.3
	30	0	76	8.8
	20	0	56	10.4
	10	0	47	23.3
	0	97	32	34.1
	−10	46	32	49
	−20	169	27	74.6
Li_6PS_5Br	60	142	51	1.1
	50	240	44	2.3
	40	0	44	4.3
	30	15	41	5.8
	20	0	43	8.6
	10	63	38	23.4
	0	0	41	37.3
	−10	87	33	50
	−20	45	36	89
$Li_{10}GeP_2S_{12}$	60	62	73	1.4
	50	69	86	3.3
	40	97	68	3.5
	30	120	57	4.1
	20	73	56	5.9
	10	614	64	26.4
	0	61	60	28.9
	−10	48	63	47.9
	−20	104	52	64.9

Table A2. Theoretical parameters obtained by fitting experimental data associated with Figure A1.

Electrolytes	Temperature (°C)	R_1 (Ω)	C_2 (pF)	R_2 (kΩ)
Li_6PS_5Cl	40	177	19	8.8
	RT	55	15	35.9
Li_6PS_5Br	40	0	16	3.2
	RT	82	12	27
$Li_{10}GeP_2S_{12}$	40	0	27	7.9
	RT	4680	24	24.4

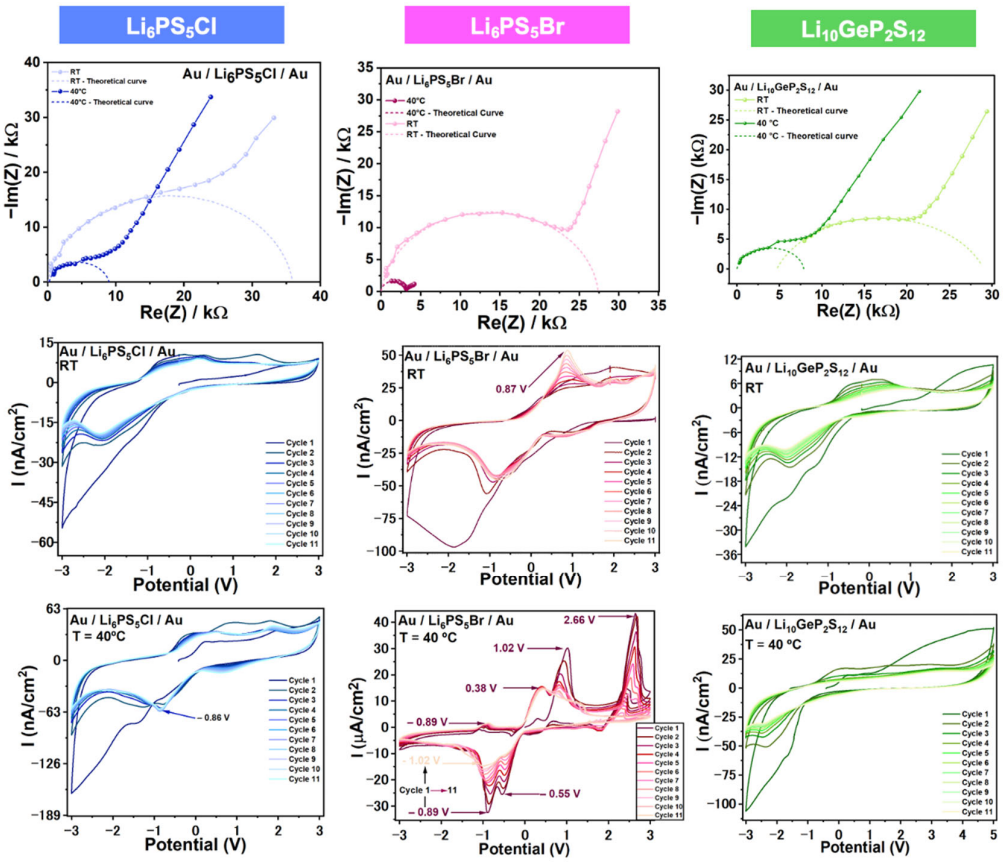

Figure A1. Complementary PEIS and CV for the Au/electrolyte/Au symmetric cells.

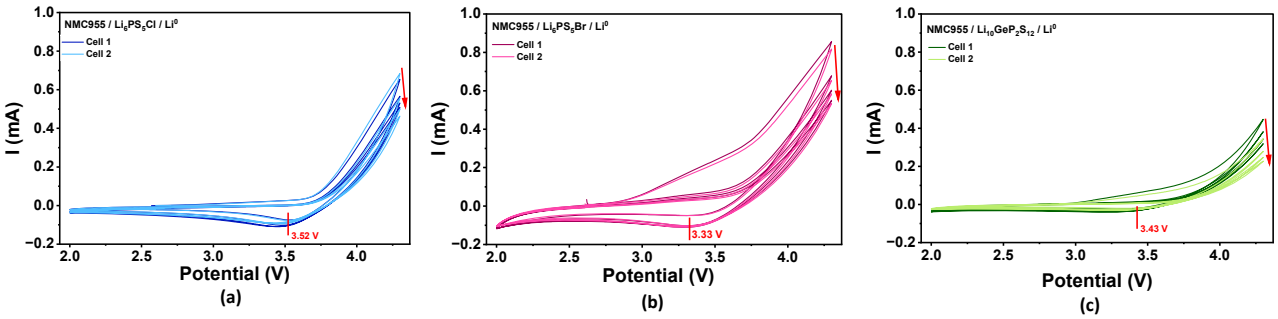

Figure A2. CV on NMC955/electrolyte/Li^0 half cells with electrolytes (**a**) LPSCl, (**b**) LPSBr, and (**c**) LGPS.

References

1. Alawi, M.J.; Gamal, H.; Rashad, M.; Alziyadi, M.O.; Shalaby, M.S. Zinc-Ion Batteries: Drawbacks, Opportunities, and Optimization Performance for Sustainable Energy Storage. *J. Alloys Compd.* **2025**, *1012*, 178455. [CrossRef]
2. Yang, X.; Luo, J.; Sun, X. Towards High-Performance Solid-State Li–S Batteries: From Fundamental Understanding to Engineering Design. *Chem. Soc. Rev.* **2020**, *49*, 2140–2195. [CrossRef]
3. Dolla, T.H.; Ajayi, S.O.; Sikeyi, L.L.; Mathe, M.K.; Palaniyandy, N. Advances in Solid-State Batteries Fabrication Strategies for Their Manufacture. *J. Energy Storage* **2025**, *106*, 114737. [CrossRef]
4. Gomes, B.M.; Moutinho, J.F.R.; Braga, M.H. A Perspective on the Building Blocks of a Solid-State Battery: From Solid Electrolytes to Quantum Power Harvesting and Storage. *J. Mater. Chem. A Mater.* **2024**, *12*, 690–722. [CrossRef]
5. Bachman, J.C.; Muy, S.; Grimaud, A.; Chang, H.H.; Pour, N.; Lux, S.F.; Paschos, O.; Maglia, F.; Lupart, S.; Lamp, P.; et al. Inorganic Solid-State Electrolytes for Lithium Batteries: Mechanisms and Properties Governing Ion Conduction. *Chem. Rev.* **2016**, *116*, 140–162. [CrossRef] [PubMed]
6. Bocharova, V.; Sokolov, A.P. Perspectives for Polymer Electrolytes: A View from Fundamentals of Ionic Conductivity. *Macromolecules* **2020**, *53*, 4141–4157. [CrossRef]
7. Daems, K.; Yadav, P.; Dermenci, K.B.; Van Mierlo, J.; Berecibar, M. Advances in Inorganic, Polymer and Composite Electrolytes: Mechanisms of Lithium-Ion Transport and Pathways to Enhanced Performance. *Renew. Sustain. Energy Rev.* **2024**, *191*, 114136. [CrossRef]
8. Murugan, R.; Thangadurai, V.; Weppner, W. Fast Lithium Ion Conduction in Garnet-Type $Li_7La_3Zr_2O_{12}$. *Angew. Chem.-Int. Ed. Engl.* **2007**, *46*, 7778. [CrossRef]
9. Deng, Y.; Eames, C.; Fleutot, B.; David, R.; Chotard, J.-N.; Suard, E.; Masquelier, C.; Islam, M.S. Enhancing the Lithium Ion Conductivity in Lithium Superionic Conductor (LISICON) Solid Electrolytes Through a Mixed Polyanion Effect. *ACS Appl. Mater. Interfaces* **2017**, *9*, 7050–7058. [CrossRef]
10. Yu, C.; Ganapathy, S.; Hageman, J.; Van Eijck, L.; Van Eck, E.R.H.; Zhang, L.; Schwietert, T.; Basak, S.; Kelder, E.M.; Wagemaker, M. Facile Synthesis Toward the Optimal Structure-Conductivity Characteristics of the Argyrodite Li_6PS_5Cl Solid-State Electrolyte. *ACS Appl. Mater. Interfaces* **2018**, *10*, 33296–33306. [CrossRef]
11. Kamaya, N.; Homma, K.; Yamakawa, Y.; Hirayama, M.; Kanno, R.; Yonemura, M.; Kamiyama, T.; Kato, Y.; Hama, S.; Kawamoto, K. A Lithium Superionic Conductor. *Nat. Mater.* **2011**, *10*, 682–686. [CrossRef] [PubMed]
12. Braga, M.H.; Stockhausen, V.; Oliveira, J.C.E.; Ferreira, J.A. The Role of Defects in Li_3ClO Solid Electrolyte: Calculations and Experiments. *Mater. Res. Soc. Symp. Proc.* **2013**, *1526*, 36–40. [CrossRef]
13. Braga, M.H.; Ferreira, J.A.; Stockhausen, V.; Oliveira, J.E.; El-Azab, A. Novel Li_3ClO Based Glasses with Superionic Properties for Lithium Batteries. *J. Mater. Chem. A Mater.* **2014**, *2*, 5470–5480. [CrossRef]
14. Xia, W.; Zhao, Y.; Zhao, F.; Adair, K.; Zhao, R.; Li, S.; Zou, R.; Zhao, Y.; Sun, X. Antiperovskite Electrolytes for Solid-State Batteries. *Chem. Rev.* **2022**, *122*, 3763–3819. [CrossRef]
15. Nie, K.; Hong, Y.; Qiu, J.; Li, Q.; Yu, X.; Li, H.; Chen, L. Interfaces Between Cathode and Electrolyte in Solid State Lithium Batteries: Challenges and Perspectives. *Front. Chem.* **2018**, *6*, 616. [CrossRef]
16. Zamperlin, N.; Cid, R.; Kekkonen, V.; Pesce, A.; Cheddadi, M.; Gomes, B.M.; Baptista, M.C.; Braga, M.H.; Orue, A.; López-Aranguren, P. Advanced Manufacturing of Thin-Film Lithium Metal Anode by Pulsed-Laser Deposition for Next-Generation Solid-State Batteries. *J. Power Sources* **2025**, *655*, 237986. [CrossRef]
17. Gomes, B.M.; Baptista, M.C.; Orue, A.; Dhrubajyoti, B.; Terlicka, S.; Sjövall, P.; Zamperlin, N.; Fonseca, C.; Smajic, J.; Kekkonen, V. All-Solid-State Lithium Batteries with NMC955 Cathodes: PVDF-Free Formulation with SBR and Capacity Recovery Insights. *Energy Mater.* **2025**, *5*, 500091. [CrossRef]
18. Ni, W. Perspectives on Advanced Lithium–Sulfur Batteries for Electric Vehicles and Grid-Scale Energy Storage. *Nanomaterials* **2024**, *14*, 990. [CrossRef]
19. Raza, H.; Bai, S.; Cheng, J.; Majumder, S.; Zhu, H.; Liu, Q.; Zheng, G.; Li, X.; Chen, G. Li-S Batteries: Challenges, Achievements and Opportunities. *Electrochem. Energy Rev.* **2023**, *6*, 29. [CrossRef]
20. Yu, C.; van Eijck, L.; Ganapathy, S.; Wagemaker, M. Synthesis, Structure and Electrochemical Performance of the Argyrodite Li_6PS_5Cl Solid Electrolyte for Li-Ion Solid State Batteries. *Electrochim. Acta* **2016**, *215*, 93–99. [CrossRef]
21. Shi, B.-X.; Weber, F.; Yusim, Y.; Demuth, T.; Vettori, K.; Münchinger, A.; Titvinidze, G.; Volz, K.; Henss, A.; Berger, R. Lithiated Polymer Coating for Interface Stabilization in Li_6PS_5Cl-Based Solid-State Batteries with High-Nickel NCM. *J. Mater. Chem. A Mater.* **2025**, *13*, 2600–2614. [CrossRef]
22. Auvergniot, J.; Cassel, A.; Ledeuil, J.-B.; Viallet, V.; Seznec, V.; Dedryvère, R. Interface Stability of Argyrodite Li_6PS_5Cl toward $LiCoO_2$, $LiNi_{1/3}Co_{1/3}Mn_{1/3}O_2$, and $LiMn_2O_4$ in Bulk All-Solid-State Batteries. *Chem. Mater.* **2017**, *29*, 3883–3890. [CrossRef]
23. Kim, T.; Kim, K.; Lee, S.; Song, G.; Jung, M.S.; Lee, K.T. Thermal Runaway Behavior of Li_6PS_5Cl Solid Electrolytes for $LiNi_{0.8}Co_{0.1}Mn_{0.1}O_2$ and $LiFePO_4$ in All-Solid-State Batteries. *Chem. Mater.* **2022**, *34*, 9159–9171. [CrossRef]

24. Singh, D.K.; Henss, A.; Mogwitz, B.; Gautam, A.; Horn, J.; Krauskopf, T.; Burkhardt, S.; Sann, J.; Richter, F.H.; Janek, J. Li_6PS_5Cl Microstructure and Influence on Dendrite Growth in Solid-State Batteries with Lithium Metal Anode. *Cell Rep. Phys. Sci.* **2022**, *3*, 101043. [CrossRef]
25. Liu, S.; Zhou, L.; Han, J.; Wen, K.; Guan, S.; Xue, C.; Zhang, Z.; Xu, B.; Lin, Y.; Shen, Y. Super Long-cycling All-solid-state Battery with Thin Li_6PS_5Cl-based Electrolyte. *Adv. Energy Mater.* **2022**, *12*, 2200660. [CrossRef]
26. Chen, Y.; Li, W.; Sun, C.; Jin, J.; Wang, Q.; Chen, X.; Zha, W.; Wen, Z. Sustained Release-Driven Formation of Ultrastable SEI Between Li_6PS_5Cl and Lithium Anode for Sulfide-Based Solid-State Batteries. *Adv. Energy Mater.* **2021**, *11*, 2002545. [CrossRef]
27. Indrawan, R.F.; Gamo, H.; Nagai, A.; Matsuda, A. Chemically Understanding the Liquid-Phase Synthesis of Argyrodite Solid Electrolyte Li_6PS_5Cl with the Highest Ionic Conductivity for All-Solid-State Batteries. *Chem. Mater.* **2023**, *35*, 2549–2558. [CrossRef]
28. Aktekin, B.; Kataev, E.; Riegger, L.M.; Garcia-Diez, R.; Chalkley, Z.; Becker, J.; Wilks, R.G.; Henss, A.; Bär, M.; Janek, J. Operando Photoelectron Spectroscopy Analysis of Li_6PS_5Cl Electrochemical Decomposition Reactions in Solid-State Batteries. *ACS Energy Lett.* **2024**, *9*, 3492–3500. [CrossRef]
29. Lee, J.; Ju, S.; Hwang, S.; You, J.; Jung, J.; Kang, Y.; Han, S. Disorder-Dependent Li Diffusion in Li_6PS_5Cl Investigated by Machine-Learning Potential. *ACS Appl. Mater. Interfaces* **2024**, *16*, 46442–46453. [CrossRef]
30. Yi, S.; Jeon, T.; Cha, G.H.; Han, Y.-K.; Jung, S.C. Unexpected Anion Segregation Enabling High Conductivity in Argyrodite $Li_{6-x}PS_{5-x}ClBrx$ Solid Electrolytes. *J. Mater. Chem. A Mater.* **2024**, *12*, 33088–33098. [CrossRef]
31. Boulineau, S.; Courty, M.; Tarascon, J.-M.; Viallet, V. Mechanochemical Synthesis of Li-Argyrodite Li_6PS_5X (X = Cl, Br, I) as Sulfur-Based Solid Electrolytes for All Solid State Batteries Application. *Solid State Ion.* **2012**, *221*, 1–5. [CrossRef]
32. Epp, V.; Gün, Ö.; Deiseroth, H.-J.; Wilkening, M. Highly Mobile Ions: Low-Temperature NMR Directly Probes Extremely Fast Li^+ Hopping in Argyrodite-Type Li_6PS_5Br. *J. Phys. Chem. Lett.* **2013**, *4*, 2118–2123. [CrossRef]
33. Sadowski, M.; Albe, K. Grain Boundary Transport in the Argyrodite-Type Li_6PS_5Br Solid Electrolyte: Influence of Misorientation and Anion Disorder on Li Ion Mobility. *Adv. Mater. Interfaces* **2024**, *11*, 2400423. [CrossRef]
34. Qu, Y.; Mateos, M.; Emery, N.; Cuevas, F.; Mercier, D.; Zanna, S.; de Anda Agustin, R.; Meziani, N.; Zhang, J. Lithium Nitridonickelate as Anode Coupled with Argyrodite Electrolyte for All-Solid-State Lithium-Ion Batteries. *J. Energy Storage* **2024**, *102*, 114027. [CrossRef]
35. Li, W.; Chen, Z.; Chen, Y.; Zhang, L.; Liu, G.; Yao, L. High-Entropy Argyrodite-Type Sulfide Electrolyte with High Conductivity and Electro-Chemo-Mechanical Stability for Fast-Charging All-Solid-State Batteries. *Adv. Funct. Mater.* **2024**, *34*, 2312832. [CrossRef]
36. Yu, C.; Hageman, J.; Ganapathy, S.; van Eijck, L.; Zhang, L.; Adair, K.R.; Sun, X.; Wagemaker, M. Tailoring Li_6PS_5Br Ionic Conductivity and Understanding of Its Role in Cathode Mixtures for High Performance All-Solid-State Li–S Batteries. *J. Mater. Chem. A Mater.* **2019**, *7*, 10412–10421. [CrossRef]
37. Chen, M.; Rao, R.P.; Adams, S. High Capacity All-Solid-State Cu–Li_2S/Li_6PS_5Br/In Batteries. *Solid State Ion.* **2014**, *262*, 183–187. [CrossRef]
38. Yu, C.; Ganapathy, S.; van Eck, E.R.H.; van Eijck, L.; Basak, S.; Liu, Y.; Zhang, L.; Zandbergen, H.W.; Wagemaker, M. Revealing the Relation Between the Structure, Li-Ion Conductivity and Solid-State Battery Performance of the Argyrodite Li_6PS_5Br Solid Electrolyte. *J. Mater. Chem. A Mater.* **2017**, *5*, 21178–21188. [CrossRef]
39. Sigar, U.; Weintraut, T.; Benz, S.L.; Engün, S.; Kremer, S.; Henss, A.; Richter, F.H. Low Resistance Interphase Formation at the PEO-LiTFSI | LGPS Interface in Lithium Solid-State Batteries. *Adv Mater Interfaces* **2025**, e00705. [CrossRef]
40. Raj, H.; Aktekin, B.; Becker, J.; Janek, J.; Pralong, V. Understanding the Role of Oxygen Substitution in Lithium Conduction and Air/Interfacial Stability of LGPS-Structured Oxy-Sulfide Electrolytes. *ACS Appl Mater Interfaces* **2025**, *17*, 48195–48208. [CrossRef]
41. Han, F.; Zhu, Y.; He, X.; Mo, Y.; Wang, C. Electrochemical Stability of $Li_{10}GeP_2S_{12}$ and $Li_7La_3Zr_2O_{12}$ Solid Electrolytes. *Adv. Energy Mater.* **2016**, *6*, 1501590. [CrossRef]
42. Jiang, P.; Zhou, H.; Song, S.; Suzuki, K.; Watanabe, K.; Yamaguchi, Y.; Matsui, N.; Hori, S.; Kanno, R.; Hirayama, M. A Composite Cathode with a Three-Dimensional Ion/Electron-Conducting Structure for All-Solid-State Lithium–Sulfur Batteries. *Commun. Mater.* **2024**, *5*, 105. [CrossRef]
43. Hassoun, J.; Verrelli, R.; Reale, P.; Panero, S.; Mariotto, G.; Greenbaum, S.; Scrosati, B. A Structural, Spectroscopic and Electrochemical Study of a Lithium Ion Conducting $Li_{10}GeP_2S_{12}$ Solid Electrolyte. *J. Power Sources* **2013**, *229*, 117–122. [CrossRef]
44. Dawson, J.A.; Islam, M.S. A Nanoscale Design Approach for Enhancing the Li-Ion Conductivity of the $Li_{10}GeP_2S_{12}$ Solid Electrolyte. *ACS Mater. Lett.* **2022**, *4*, 424–431. [CrossRef] [PubMed]
45. Umeshbabu, E.; Zheng, B.; Zhu, J.; Wang, H.; Li, Y.; Yang, Y. Stable Cycling Lithium–Sulfur Solid Batteries with Enhanced Li/$Li_{10}GeP_2S_{12}$ Solid Electrolyte Interface Stability. *ACS Appl. Mater. Interfaces* **2019**, *11*, 18436–18447. [CrossRef]
46. Zhang, N.; He, Q.; Zhang, L.; Zhang, J.; Huang, L.; Yao, X. Homogeneous Fluorine Doping toward Highly Conductive and Stable $Li_{10}GeP_2S_{12}$ Solid Electrolyte for All-Solid-State Lithium Batteries. *Adv. Mater.* **2024**, *36*, 2408903. [CrossRef]
47. Gomes, B.M.; Holtz, J.; Pinto, M.L.; Braga, M.H. Polaronic and Electrochemical Signatures in Group IVB (Ti, Zr, Hf) Oxides: Unified SKP–DFT Insights for Tunable Transport in Energy and Electronic Devices. *Adv. Funct. Mater.* **2026**, *36*, e09853. [CrossRef]

48. Baptista, M.C.; Vale, A.B.; Costa, J.M.; Braga, M.H. Robust All-Solid-State Batteries with Sodium Ion Electrolyte, Aluminum and Additive Manufacturing Inconel 625 Electrodes. *Molecules* **2025**, *30*, 4465. [CrossRef]
49. Zhou, N.; Zhang, S.; Yao, Y.; Wen, Y.; Wang, C.; Zhang, K.; Li, Y.; Hu, J.; Yang, B.; He, Y.; et al. Ionic Liquids in Quasi-Solid-State Li–S Batteries with Sulfide-Based Solid Electrolytes: A Density Functional Theory and Ab Initio Molecular Dynamics Study. *J. Phys. Chem. C* **2026**, *130*, 43–63. [CrossRef]
50. Hao, W.; Lee, M.; Hwang, G.S. First-Principles Assessment of Chemical Lithiation of Sulfide Solid Electrolytes and Its Impact on Their Transport, Electronic and Mechanical Properties. *J. Power Sources* **2023**, *560*, 232689. [CrossRef]
51. Yang, J.; Falletta, S.; Pasquarello, A. Range-Separated Hybrid Functionals for Accurate Prediction of Band Gaps of Extended Systems. *NPJ Comput. Mater.* **2023**, *9*, 108. [CrossRef] [PubMed]
52. Materials Explorer-Li_6PS_5Cl-Mp-985592. Available online: https://legacy.materialsproject.org/materials/mp-985592/ (accessed on 1 July 2025).
53. Materials Explorer-Li_6PS_5Br-Mp-985591. Available online: https://legacy.materialsproject.org/materials/mp-985591/ (accessed on 1 July 2025).
54. Materials Explorer-$Li_{10}GeP_2S_{12}$-Mp-696138. Available online: https://legacy.materialsproject.org/materials/mp-696138/ (accessed on 1 July 2025).
55. Maia, B.A.; Gomes, B.M.; Guerreiro, A.N.; Santos, R.M.; Braga, M.H. Cathodes Pinpoints for the Next Generation of Energy Storage Devices: The $LiFePO_4$ Case Study. *J. Phys. Mater.* **2024**, *7*, 025001. [CrossRef]
56. Cao, M.; Xiong, D.-B.; Yang, L.; Li, S.; Xie, Y.; Guo, Q.; Li, Z.; Adams, H.; Gu, J.; Fan, T.; et al. Ultrahigh Electrical Conductivity of Graphene Embedded in Metals. *Adv. Funct. Mater.* **2019**, *29*, 1806792. [CrossRef]
57. Braga, M.H. Coherence in the Ferroelectric A_3ClO (A = Li, Na) Family of Electrolytes. *Materials* **2021**, *14*, 2398. [CrossRef]
58. Braga, M.H.; Guerreiro, A.N. The HfO2 Ferroelectric–Metal Heterojunction and Its Emergent Electrostatic Potential: Comparison with ZrO_2 and SiO_2. *J. Mater. Chem. C Mater.* **2024**, *12*, 19386–19397. [CrossRef]
59. Kresse, G.; Hafner, J. Ab Initio Molecular Dynamics for Liquid Metals. *Phys. Rev. B* **1993**, *47*, 558. [CrossRef]
60. Materials Design, Inc. *MedeA Version 3.7.0*; Materials Design, Inc.: San Diego, CA, USA, 2025.
61. Madsen, G.K.H.; Singh, D.J.; BoltzTraP. A Code for Calculating Band-Structure Dependent Quantities. *Comput. Phys. Commun.* **2006**, *175*, 67–71. [CrossRef]